



Wearable and flexible thin film thermoelectric module for multi-scale energy harvesting

Vaithinathan Karthikeyan^a, James Utama Surjadi^b, Joseph C.K. Wong^c, Venkataraman Kannan^d, Kwok-Ho Lam^e, Xianfeng Chen^f, Yang Lu^b, Vellaisamy A.L. Roy^{g,**}

^a State Key Laboratory for Millimeter and Terahertz Waves and Department of Materials Science & Engineering, City University of Hong Kong, Kowloon Tong, Hong Kong

^b Department of Mechanical Engineering, City University of Hong Kong, Kowloon Tong, Hong Kong

^c Department of Architecture and Civil Engineering, City University of Hong Kong, Kowloon Tong, Hong Kong

^d SCSVMV University, Kanchipuram, India

^e Department of Electrical Engineering, The Hong Kong Polytechnic University, Hung Hom, Hong Kong

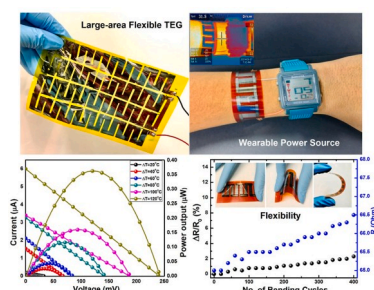
^f School of Engineering, Institute for Bioengineering, The University of Edinburgh, King's Buildings, Mayfield Road, Edinburgh, United Kingdom

^g James Watt School of Engineering, University of Glasgow, Glasgow, United Kingdom

HIGHLIGHTS

- Highly flexible and shape conformable thin-film TEG for waste heat recovery.
- Thermoelectric module as a wearable electronic gadget for human exoskeleton.
- Multi-scale Thermoelectric energy harvesting with max. power density of 8.5 mW/cm².
- Thermal touch sensor panel possessing high sensor responsivity of 0.29 μ V/W.

GRAPHICAL ABSTRACT



ARTICLE INFO

Keywords:

Flexible thermoelectric generator
Wearable electronics
Thermal sensor
Thin films

ABSTRACT

Developing a thermoelectric generator (TEG) with shape conformable geometry for sustaining low-thermal impedance and large temperature gradient (ΔT) is fundamental for wearable and multi-scale energy harvesting applications. Here we demonstrate a flexible architectural design, with efficient thin film thermoelectric generator as a solution for this problem. This approach not only decreases the thermal impedance but also multiplies the temperature gradient, thereby increasing the power conversion efficiency (PCE) as comparable to bulk TEG. Intact thin films of Tin telluride (p-type) and Lead Telluride (n-type) are deposited on flexible substrate through physical vapor deposition and a thermoelectric module possessing a maximum output power density of 8.4 mW/cm² is fabricated. We have demonstrated the performance of p-SnTe/n-PbTe based TEG as a flexible wearable power source for electronic gadgets, as a thermal touch sensor for real-time switching and temperature monitoring for exoskeleton applications.

* Corresponding author.

E-mail address: Roy.Vellaisamy@glasgow.ac.uk (V.A.L. Roy).

<https://doi.org/10.1016/j.jpowsour.2020.227983>

Received 3 December 2019; Received in revised form 7 February 2020; Accepted 29 February 2020

Available online 9 March 2020

0378-7753/© 2020 Elsevier B.V. All rights reserved.

1. Introduction

Wearable electronic devices (e-wearables) are one of the most important among the emerging end-user technologies [1,2]. With e-wearables, real-time and continuous monitoring of daily human physical and biological activities like fitness, heartbeat rate, blood pressure, body temperature, entertainment, navigation and several other features are made possible [3,4]. An ultra-light, flexible and shape conformable skin-interfaced systems is the current research focus to overcome the key challenges in conventional wearables [5,6]. Wearable electronic devices generally require a stable, reliable and durable power source for effective functioning. Handy battery unit fixed inside the system has become one of the bottleneck problems in wearable electronic systems [7,8]. Presently, lithium-ion batteries are mostly used as power sources which cannot be an everlasting source of power and are often reported as reason for battery explosions [9]. Moreover, disassembling for frequent charging and replacement of batteries are inconvenient and causes loss of data collection duration for the wearers. Therefore, there is an urgent need to meet the market demands of developing a lightweight, eco-friendly and long-lasting source for self-powering e-wearables [10–12]. For this, Self-powering nanotechnologies provide a unique solution with superflexible, cost-effective, high performing battery free electronic devices by directly harvesting and converting body heat into electricity for powering the e-wearables [13,14]. Thermoelectric generators (TEGs) can efficiently convert heat energy directly into electrical energy with vibration-less, emission-free eco-friendly approach [15]. Thermoelectric or Seebeck effect developed by using thermoelectric materials can continuously power the e-wearables by harvesting the heat energy. The thermoelectric power generation is determined by the figure of merit of a thermoelectric (TE) material, which is defined as $S^2\sigma T/K$, where S , σ , K and T are Seebeck coefficients, electrical conductivity, thermal conductivity and absolute temperature, respectively. From this equation, it is apparent that a high zT can be achieved by increasing the power factor ($S^2\sigma$) and reducing the thermal conductivity (K) of the material [16,17]. Moreover, the thermoelectric power output of the device is directly proportional to the square of the temperature difference applied across it. Sustaining the thermal gradient in the device depends on the heat absorption, dissipation and heat resistance of the TE materials and also device design [18,19]. Over longtime, conventional Bismuth Telluride based TEG is widely used as a power generator and peltier modules because of constant optimization efforts. However, conventional TEGs suffers from a rigid and brittle structure which limits their surface contact area and thus reduces heat recovery efficiency [20]. In this aspect, low-dimensional thin TE materials can realize higher zT than their bulk counterpart due to their low thermal conductivity associated with quantum confinement effect [21–23]. Meanwhile, thin film thermoelectric devices use less amount of materials compared to bulk thermoelectric generator (TEG) and provides easy integration with integrated circuits [24,25]. The design of TEG can usually be categorized into in-plane and cross-plane structures [26]. Many works have been reported on cross-plane bismuth telluride based thin film through electrodeposition [27], screen printing [28], brush-painting [29,30] and inkjet printing [31]. In comparison, an in-plane TEG structure is mechanically stronger and more flexible and conformable over a hot surface [32–35]. However, the electrical conductivity of the thin film TE devices is reduced due to grain boundary scattering. Therefore, one challenge is to fabricate films with higher electrical conductivity and lower thermal conductivity, thereby enabling high zT for efficient power generation. Firstly, the basic requirements for a good thermoelectric module needs to be satisfied for efficient use in practical applications. Consistent materials with excellent TE performance, high mechanical stability and flexibility should be developed [18]. Then, easy large scale production methods with low fabrication cost need to be adopted [29]. Finally, novel module designs concerning with wearable, portability and flexibility for better integration with the heat source for high power

output should be established [36,37]. Appropriate to the above said requirements, Metal Tellurides like Tin telluride and Lead telluride are very well explored for their metallic glass property with high electrical conductivity in the thermoelectric community. Both SnTe and PbTe are cubic structured direct narrow bandgap semiconductor with 0.18 eV and 0.32 eV respectively [38–41]. Recently, the bulk performance of SnTe and PbTe are much higher than conventional Bi_2Te_3 with $zT \sim 2$ [42–45]. Thin films of these materials are also well explored for better thermoelectric performance, with much lower electrical resistivity than Bi_2Te_3 thin films [46,47]. Thus thin film TEGs fabrication with this material and conformable substrates can increase the device power conversion efficiency.

Here in this work, we demonstrate an in-plane wearable and multi-scale flexible metal telluride based thermoelectric generator with high current and power density. In our device, a thin film of p-SnTe and n-PbTe are thermally deposited onto a flexible polyimide substrate interconnected with aluminum as contact to form the thermoelectric generator structure. The temperature-dependent electrical and thermal properties of the deposited films were studied. Our tests demonstrate that the device characteristic load test shows the capacity for producing a current and power density of 34.7 mA/cm² and 8.4 mW/cm², respectively, at the maximum working temperature of 120 °C. The infrared images and the power density observation exhibits the ability of thin films to sustain a large temperature gradient.

2. Materials and methods

Device Fabrication: Fig. 1a shows the schematic fabrication process of a thermoelectric generator. First, n-PbTe and p-SnTe arrays with a thicknesses of 100 nm are deposited as n-type and p-type legs, respectively, on a clean flexible polyimide substrate at room temperature by thermal evaporation of high purity (99.99%) SnTe and PbTe pieces. The deposition was performed at a working pressure of $\sim 5 \times 10^{-6}$ mBar and deposition rate of ~ 10 Å/s and ~ 15 Å/s for SnTe and PbTe, respectively. The deposition of each p- and n-type legs with specified dimensions was done through a specially designed metal-shadow mask over the polyimide substrate of 500 μm thickness. Through these procedures, a SnTe–PbTe based TEG with 4 p-n pairs interconnected by aluminum film of 50 nm was fabricated. The advantages of thermal evaporation technique are higher film deposition rates, purity of the film deposited under high vacuum and reduced surface damage to the substrate, unlike sputtering.

Thin film material characterization: X-ray diffraction patterns of p-SnTe and n-PbTe thin films were performed by Rigaku SmartLab diffractometer. The Raman scattering phonon modes of the fabricated thin films were analyzed using inVia Renishaw Raman spectrometer with a 633 nm laser source. The surface morphologies of the deposited films were characterized by Quanta FEG 450 SEM. The surface roughness and grain size were studied through atomic force microscopy (AFM) in contact mode. The Scanning Transmission Microscopy profile of PbTe and SnTe thin films were simulated using CASTEP module in Material studio 8.0. The stoichiometry and elemental analysis of the deposited films were confirmed by Bruker X-ray fluorescence (XRF). The hardness and modulus of the PbTe and SnTe thin films with thicknesses ranging from 100 nm to 500 nm were measured via nanoindentation using a Bruker TI950 Tribo Indenter with a standard Berkovich tip. Displacement-controlled mode was used with a constant strain rate of 0.01 s^{−1} at room temperature. Hardness and modulus of the thin films were measured at a series of indentation depths and calculated using the classic Oliver-Pharr method. The temperature-dependent measurement of the electrical properties was analyzed through ECOPIA hall measurement system using Van der Pauw 4-terminal method. The thermoelectric Seebeck voltage of the p- and n-type thin films was determined by measuring the open circuit voltage at an applied temperature difference by resistive heaters.

Thermoelectric performance analysis: The voltage and temperature

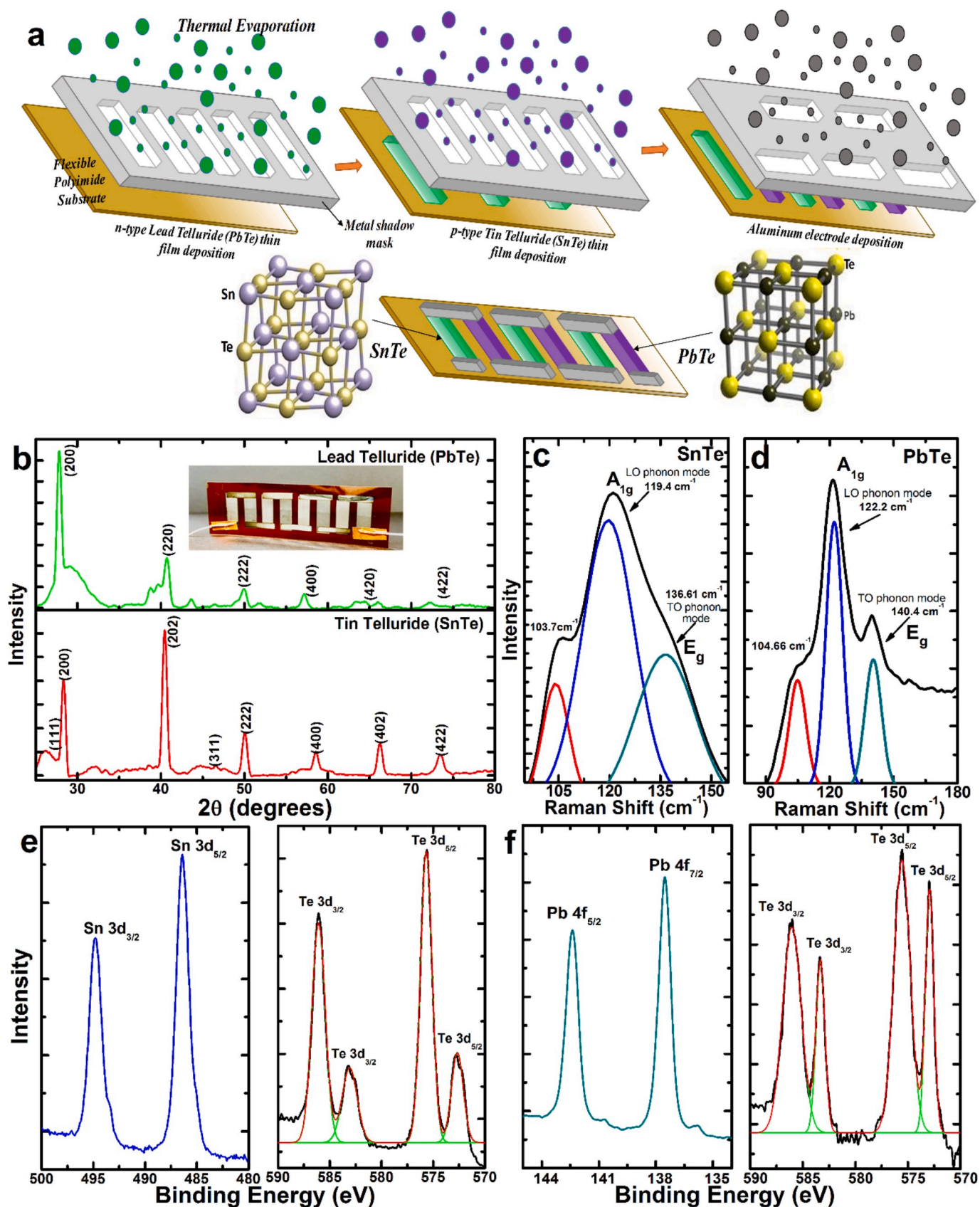


Fig. 1. (a) The schematic diagram shows the steps involved in TEG fabrication (b) XRD pattern of the deposited PbTe and SnTe thin film with their lattice orientation (c) and (d) show the Raman scattering and phonon modes of the deposited SnTe and PbTe thin films. (e) and (f) shows the high-resolution X-ray photoelectron spectroscopy scan for SnTe and PbTe thin films respectively.

gradient across the device were measured using a K-type thermocouple with Keithley 6517A Electrometer. The thermal conductivity of SnTe and PbTe thin films were measured by Netzsch Light Flash apparatus LFA 467 Hyperflash which provides ultra-fast sampling rate for thin film samples. The infrared image demonstrating the temperature difference was determined from a FLIR E33 series infrared thermal imaging camera with an accuracy of up to $\pm 2^\circ\text{C}$. The temperature-dependent TEG output P-V characteristics were obtained by sweeping the load resistance and recording the corresponding change in voltage and current from the Keithley 6517A controlled by Labtrace 2.0 software. To further study the real-time performance of the TEG, three TEG devices were connected in series over a circular alumina pipe attached to a hot air output of 300°C and then the corresponding voltage and current output were recorded using a multimeter.

3. Results and discussion

Fig. 1b shows the XRD patterns of the deposited PbTe and SnTe thin films which indicate their phase purity and crystallinity. The XRD patterns suggest the formation of a single phase cubic SnTe with a dominant characteristic peak (200) (*Fm3m*, JCPDS card #08-0487) and cubic fcc NaCl-type PbTe structure with the orientation along (200) (JCPDS card

#77-0246) [48,49]. The grain size of the deposited thin films was evaluated by Debye-Scherrer's equation ($D = k\lambda/B \cos\Theta$) and the values are 23.9 and 17.44 nm for SnTe and PbTe, respectively. The lattice constants calculated from the XRD pattern are 6.300 and 6.484 Å for SnTe and PbTe, respectively, which is in good agreement with the standard values. The smaller grain size ensures the formation of uniform and imperfect free crystalline thin film deposition. For deep structural understanding of the deposited thin metal tellurides, Raman scattering measurements were subsequently performed. In the Raman scattering spectra in Fig. 1c-d, the low-frequency vibrational modes are observed in layered metal chalcogenide materials because of the strong coupling between their interlayers [50]. Generally, telluride-based materials exhibit predominant peaks at 119 cm^{-1} and 139 cm^{-1} which are attributed to the optical phonon and transverse optic modes. In line with this, the Raman spectrum of the SnTe thin film shows the peaks at 103.8, 119.4 and 136.61 cm^{-1} similar to their bulk equivalent [50]. The Raman spectrum of the SnTe film is dominated by longitudinal optical (LO) modes at 119.4 cm^{-1} and transverse optical (TO) phonons at 136.61 cm^{-1} , whereas the shoulder peak at 103.8 cm^{-1} arises from the low energy part of the TO phonon mode. Similarly, the Raman spectrum of the PbTe film also exhibits equivalent peaks at 104.6, 122.2 and 140.4 cm^{-1} [51]. XPS measurements were performed to analyse the

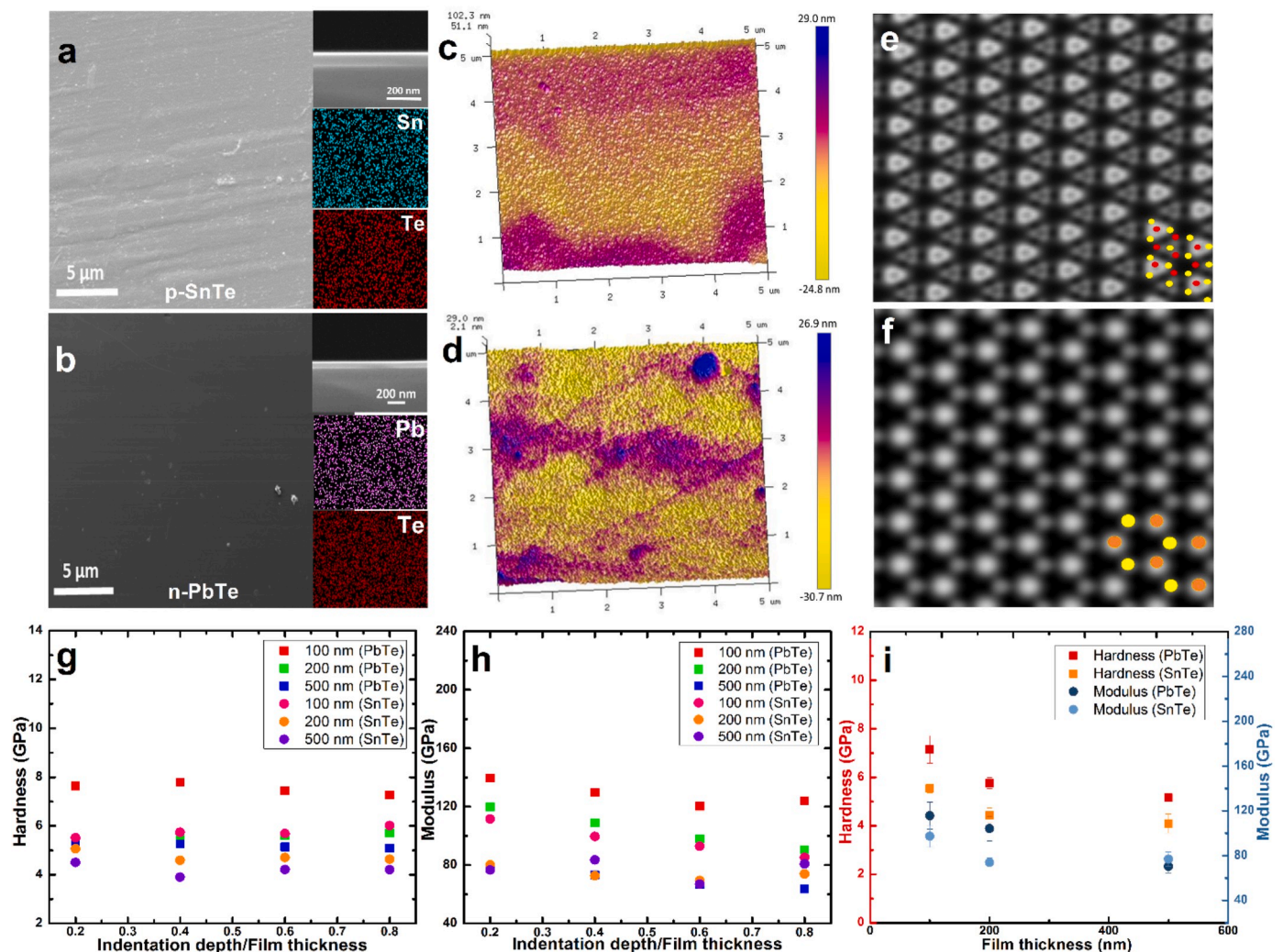


Fig. 2. (a) and (b) are the SEM images, showing the surface morphology of p-SnTe and n-PbTe with the inset images showing their thin-film cross-section and elemental mapping respectively; (c) and (d) are the AFM surface morphology images of SnTe and PbTe respectively; (e) and (f) are the theoretically simulated STM pattern (red dots represent Sn atoms and orange and yellow dots represent Pb and Te atoms, respectively); (g) and (h) compares the hardness and Young's modulus of the thin films with respect to Indentation depth/Film thickness, (i) shows the thin film thickness dependent hardness and young's modulus. (For interpretation of the references to colour in this figure legend, the reader is referred to the Web version of this article.)

composition of the deposited thin films, as shown in Fig. 1e–f, the high resolution scan for the SnTe and PbTe thin films show the presence of peaks at 487.2 eV and 495.5 eV match to core emission levels of Sn 3d_{5/2} and Sn 3d_{3/2}, the peaks at 137.6 eV and 143 eV correspond to the Pb 4f_{7/2} and Pb 4f_{5/2} and the peaks at 571 eV and 582.6 eV match to core emission levels of Te 3d_{5/2} and Te 3d_{3/2} respectively. The XPS measurements reveal the quality of the deposited thin films.

The surface morphology of the deposited p-SnTe and n-PbTe films were characterized by field emission scanning electron microscopy and the results are presented in Fig. 2a–b. The deposited films exhibit a smooth surface without any specific morphological growth. The FESEM surface morphology shows the development of densely packed uniform metallic film without any pin holes or abnormal grain growth on the surface. The inset cross-sectional FESEM of thin film shows intact deposition of thin film on the substrate. Elemental mapping for SnTe and PbTe shows uniform distribution of elements on the film surface without any over accumulation patterns. Further, from XRF measurement, we observed that the peaks of elements Sn and Te have an elemental composition of 48.18% and 51.82%, whereas the peaks of elements Pb

and Te shows 61.88% and 38.12% composition. The XRF results indicate the formation of perfect stoichiometry in both p-SnTe and n-PbTe thin films with highly crystalline structures. The theoretical simulation on the STM profile using CASTEP model was calculated where the tunnel electrons flow from the occupied orbitals of the scanning tip to the empty states of the sample on applying a positive bias [52]. The calculated STM image with positive bias corresponds to the valence band which is acquired from the electronic density difference at the Fermi level of the material [53]. The calculated STM profile for the SnTe and PbTe at an applied bias voltage of +2 V are as shown in Fig. 2e–f, respectively. From the simulated STM profile, we are able to visualize the arrangement of elements in the thin film at room temperature [54]. For a deep understanding of the roughness profile of the deposited thin film, AFM measurements were performed and the results are shown in Fig. 2c–d. The AFM images indicate that the deposition of nano-textured surface morphology with a mean roughness of 6.10 and 5.79 nm for SnTe and PbTe, respectively. Surface roughness plays a significant role in controlling the electrical and thermal conductivity of the material because the dense thin film surface moderates the surface scattering and

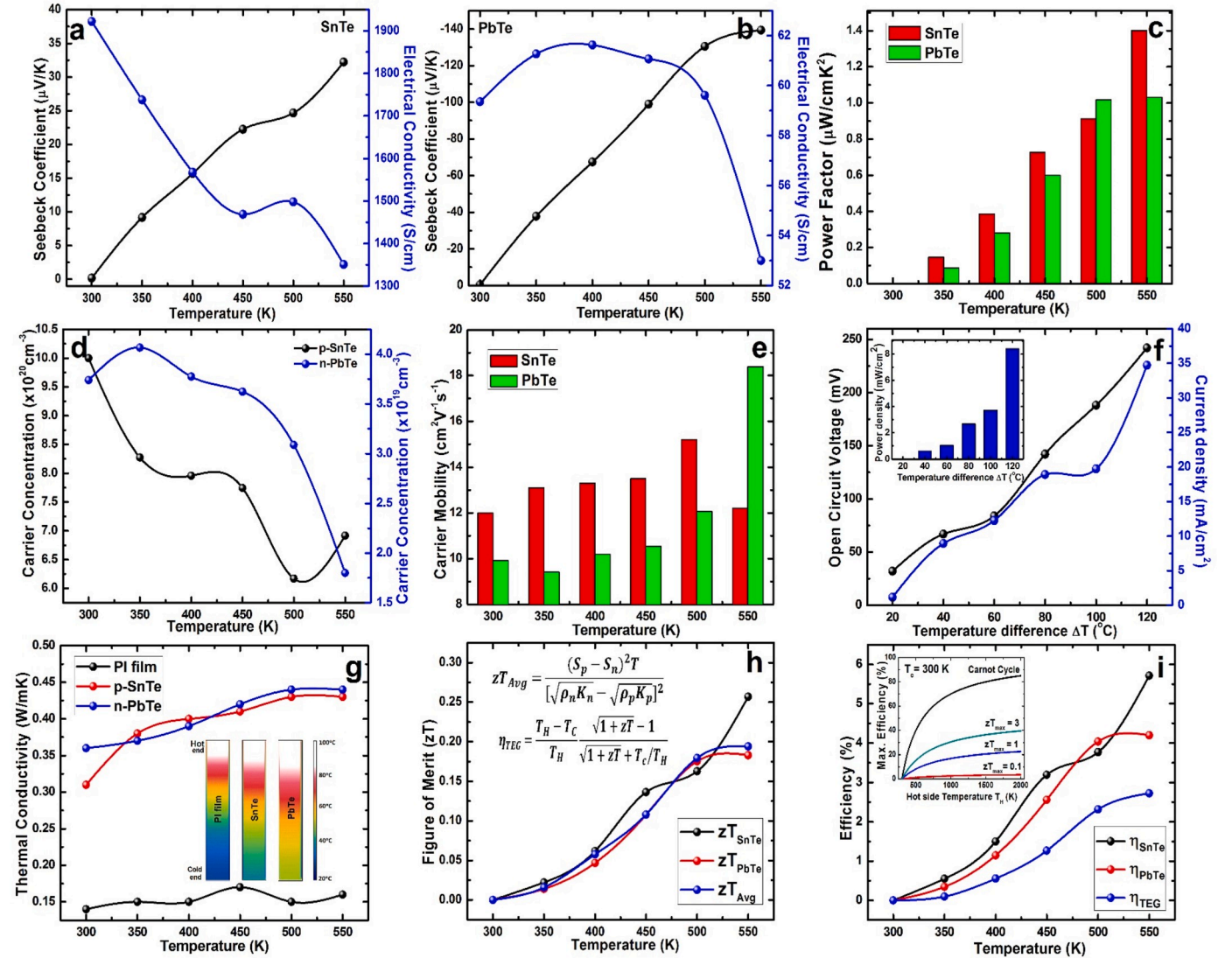


Fig. 3. (a) and (b) shows the temperature-dependent seebeck coefficient and Electrical conductivity of the deposited thin film (c) explains the power factor($s^2\sigma$) changes for p- and n-type samples. (d) and (e) shows the temperature-dependent carrier density and mobility (f) demonstrates the V_{oc} and J_{sc} of the fabricated TEG with insight image showing the attained power density (g) shows the thin film thermal conductivities (insight image is the heat transfer pattern in the thin film between hot and cold side simulated using Energy2D software [66]) (h) demonstrates the achieved maximum figure of merit (zT) for the thin film TEG (i) shows the efficiency of the thin film TE material and TEG (the insight plot compares the carnot engine efficiency with TEG's zT).

hinders the phonon transport resulting in lower thermal conductivity [55]. From the AFM analysis, we observe that the deposited film has a compact nano-textured surface with a uniform roughness and height profile suiting well for thermoelectric performance. The temperature-dependent electrical properties and Seebeck coefficient of the deposited metal telluride thin films are shown in Fig. 3. The in-plane electrical conductivity of SnTe decreases with an increase in temperature, which can be associated with the increase in carrier scattering due to lattice vibrations. A similar effect is observed in the case of PbTe thin film. However, the electrical conductivity of PbTe is much lower than that of SnTe. This change in the electrical conductivity can be understood from the hall measurement results in Fig. 3c–d.

Nanoindentation studies on the thin films were performed to analyse the thickness dependent hardness and young's modulus. Fig. 2g–h exhibit the hardness and Young's modulus of the PbTe and SnTe thin films at different indentation depths normalized by the film thickness. From Fig. 2i, it could be seen that the maximum hardness and Young's modulus are recorded for 100 nm thickness of SnTe and PbTe respectively; which could be attributed to the better surface quality/reduced roughness. Furthermore, the 100 nm PbTe and SnTe films show no apparent cracking and significant degradation of electrical conductivity upon multiple bending cycles (~2.3% change in resistance between 1st and 400th cycle). In contrast, the 200 nm and 500 nm films (Supplementary Fig. S2) show obvious micro-cracks upon cyclic bending, which considerably decreases its electrical conductivity (~6.5% and ~13% change in internal resistance of TEG for 200 nm and 500 nm films, respectively). The cracking of thermoelectric thin films upon mechanical loading has also been observed in other thin film generators and is a major concern for device stability. As such, the results imply that 100 nm is the optimum thickness for the flexible and wearable thermoelectric generator [56,57]. Temperature-dependent hall measurement shows the maximum carrier concentrations are $9.9 \times 10^{20} \text{ cm}^{-3}$ and $4 \times 10^{19} \text{ cm}^{-3}$ for SnTe and PbTe, respectively. The carrier concentration for both SnTe and PbTe decreases with increase in mobility corresponding to temperature rise. This phenomenon of increase in carrier mobility with temperature shows the absence of scattering points due to the nano-textured grains and surface roughness of the deposited film [21]. The obtained results agree with the Petritz-mobility model explaining the temperature-dependent relationship between grain boundaries and carrier transportation [58,59]. In general, the thermoelectric property of a material depends solely on their carrier transport mechanisms. Consequently, the Seebeck coefficients are modified from their bulk counterpart depending on potential barriers, grain boundary scattering and imperfections. The Seebeck coefficient of the thin films shows a maximum of 36 $\mu\text{V/K}$ and $-140 \mu\text{V/K}$ at 550 K and power factors of 1.4 $\mu\text{W/cmK}^2$ and 1.1 $\mu\text{W/cmK}^2$ for SnTe and PbTe, respectively. The Seebeck coefficient follows an increasing trend and exposes its interdependency on electrical conductivity. The properties of thermoelectric materials are varying at different layer thicknesses owing to the electron-phonon interactions at ever gradient temperature. In this aspect, power factor of SnTe and PbTe at room temperature are higher than the conventional bismuth telluride thin films [60]. The thin film thermal conductivity depends purely on the nano-textured gains rather than the strain effect in bulk materials. Under relaxation time approximation, the thickness and grain size dependent phonon relaxation time (including dislocations, point defects, phonon-phonon scattering and grain boundary scattering) τ_c is derived from Callaway's model [61] as:

$$\tau_c^{-1} = \frac{c}{D} + \frac{c}{t} + A\omega^4 + B\omega^2 T \exp\left(-\frac{\theta_p}{3T}\right) + C\omega$$

where D and t are the grain size and film thickness. In the case of thin film materials, the heat flow is parallel to the film surface which offers the possibility of decoupling the electronic and thermal transport. Fig. 3g compares the total thermal conductivity of the PI film substrate with the deposited SnTe and PbTe thin films. The obtained thermal

conductivity shows a slight increasing trend with temperature, revealing the absence of scattering points. The thermal conductivities of SnTe and PbTe are 0.31 W/mK and 0.36 W/mK at 300 K, while the PI substrate shows a relatively constant thermal conductivity of ~0.15 W/mK between 300 and 550K. From the thermal and electrical measurements, the figure of merit (zT) was calculated from $S^2\sigma/T$ and the results are presented in Fig. 3h. The maximum zT is ~0.3 (p-type) and ~0.2 (n-type) for SnTe and PbTe at 550 K, respectively. We have also calculated the total average figure of merit of the fabricated thermoelectric generator using the relation [62]:

$$zT_{avg} = \frac{(S_p - S_n)^2 T}{[\sqrt{\rho_n K_n} - \sqrt{\rho_p K_p}]^2}$$

where S_p and S_n are seebeck coefficient of p and n type respectively. Similarly, ρ and K are electrical resistivity and thermal conductivity respectively.

The maximum total average figure of merit zT_{Avg} of the thermoelectric generator is determined as ~0.2 at 550 K as shown in Fig. 3h. This favorable zT values arises from the enhanced electrical and ultra-low thermal conductivities of the deposited thin films. In the view of the maintained temperature difference between the hot and cold side due to the conformable in-plane TEG design, we estimated the p and n type material efficiency along with the total TEG efficiency as shown in the Fig. 3i. The individual leg's and the TEG efficiency is calculated from the formula [63]:

$$\eta_{TEG} = \frac{T_H - T_C}{T_H} \frac{\sqrt{1 + zT} - 1}{\sqrt{1 + zT} + T_C/T_H}$$

where T_H and T_C are the hot side and cold side temperature. Maximum efficiency of p and n-type material thin film are calculated as 5.71% and 4.19% at 550 K respectively. From the TEG zT_{Avg} , the total device efficiency is determined as 2.72%. Further comparing the efficiency of Carnot engine with range of figure of merit ($zT = 0.1, 1$ and 3), we demonstrate the equivalent performance of our fabricated SnTe–PbTe based thin film TEG in the temperature range of 300–550K. Moreover, these values reported are the highest among any thin film based TEGs.

Thermoelectric performance of flexible in-plane p-SnTe/n-PbTe generators:

We demonstrate our deposited SnTe and PbTe thin film device has a high value of the figure of merit due to the enhanced electrical and ultra-low thermal conductivities, the most important step is to explore its real-time performance as a TE generator. Firstly, we used the thin films to make a wearable electronic power source and the measurement shows that 5.3 mV can be generated from body heat at a normal body temperature (Fig. 4a) and it is enough to power a wrist watch by storing the power output from the TEG through external circuit (Fig. 4b).

The corresponding infrared image explains the temperature gradient applied over the TEG. We measured the output open circuit voltage and current density of the TE generator consisting of 4 pairs of p-n legs interconnected by aluminum contacts as shown in Fig. 3f. At a temperature difference (ΔT) of 120 °C, the maximum open circuit voltage and current density of 250 mV and 34 mA/cm² were recorded. Furthermore, in order to study the real-time load characteristics of the fabricated TE generator, the current-voltage-power characteristics were measured with varying temperature differences from 20 to 120 °C, as shown in Fig. 4g. The output power is measured for different external resistance, where the maximum peak power output of 366 nW is obtained at ΔT of 120 °C. The P–V curve shows a characteristics increase in the output power at each increase of temperature difference (ΔT). Thus the TE generator shows a maximum performance at 120 °C with 250 mV and 6 μA which is the highest recorded for any reported in-plane TEG [32–34,64,65]. Additionally, to demonstrate the real-time daily life/-industrial application of the fabricated flexible TEG we performed the testing with different types of heat source. We connected three TEGs in

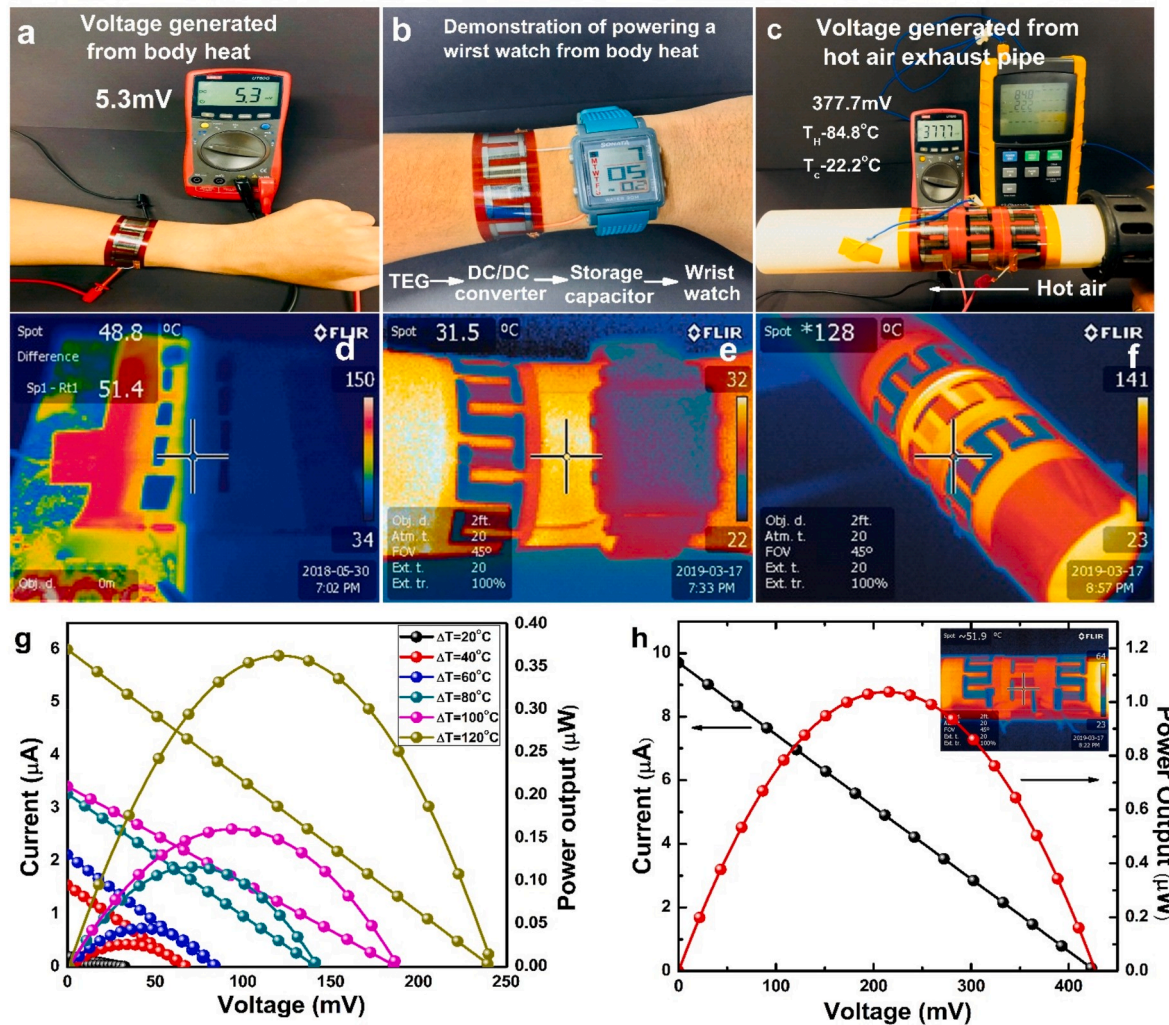


Fig. 4. Real-time applications (a) shows the capability of the TEG to generate voltage (mV) from human body heat (b) demonstrates the possibility of fabricated TEG as a flexible wearable electronics to replace batteries (c) shows the industrial high temperature power harvesting capability from heat exchangers. (d), (e) and (f) are the infrared images of TEG under various heat sources demonstrating the capacity of TEG to maintain temperature gradient (g) show the load characteristics performance of a single TEG under varied temperature gradients (h) load characteristic performance of serially connected TEGs over an alumina pipe with a temperature gradient of 120 °C.

series over a hot air exhaust pipe surface as shown in the Fig. 4c, where we recorded a constant voltage and current of up to 500 mV and 10 μA as shown in the load characteristic curve in Fig. 4h. Fig. 4g and h shows the performance of the TEG for industrial application as waste heat harvesting source for achieving energy efficiency. The infrared images clearly demonstrate the metallic glass property of the thin Film TE materials in maintaining the temperature gradient. Thus further on increasing the surface area of the device we can harvest a huge amount of heat wasted in the surroundings. For substantiating the direct conversion human waste heat into electricity, the fabricated large-area TEG with active device area of 50 cm^2 and 32 p-n TE pairs was wrapped around the human wrist, which efficiently powered an LED light with low intensity. The generated voltage corresponds to the temperature difference between the human wrist and the ambient environment ($\Delta T = 10^\circ\text{C}$) which is stabilized with LTC 3108 energy harvester circuit to power the LED. The performance stability of the TEG under heating and cooling cycles were analyzed by continuously measuring the change in internal resistance of the device.

Fig. 5c shows the device stability over 150 thermal cycles both over flat and curved surfaces, where the internal electrical resistance of the device remains stable without any significant changes. Fig. 5d demonstrates the flexibility of fabricated thermoelectric thin films over the

polyimide substrates, the stability of the internal resistance with respect to the bending radius (3–5 cm) of the device were also studied. The change in internal resistance of the TEG does not change significantly (less than $\sim 2.5\%$) under simultaneous flat and bend conditions over 400 cycles, which is appropriate for practical applications. While the internal resistance of the TEG with 200 nm and 500 nm thick films drastically increase with the number of bending cycles as shown in supplementary information S4.

To demonstrate the excellent biothermal sensing property of the fabricated TEG, we fabricated a thermal touch sensor panel by sandwiching the p-SnTe layer with n-PbTe layer with copper contacts (Fig. 6a). With this setup, we detect the finger touch on the device by measuring the change in voltage and current induced by the human skin temperature. The heat transfer between the finger and sensor surface creates a temperature gradient on the material interface leading to the generation of impulse current. The sensor responsivity over wide range if temperature was calculated as 0.29 $\mu\text{V}/^\circ\text{C}$. Fig. 6e shows the response of the sensor with and without heat input over a duration of 60 s, the detected heat pulse's intensity corresponds to the heat applied from the fingertip. The rise and fall time of the heat pulse signal are 150 ms and 200 ms respectively. The sharp rise and fall of the detected heat pulse prove efficient detection without any time lag, this property arises from

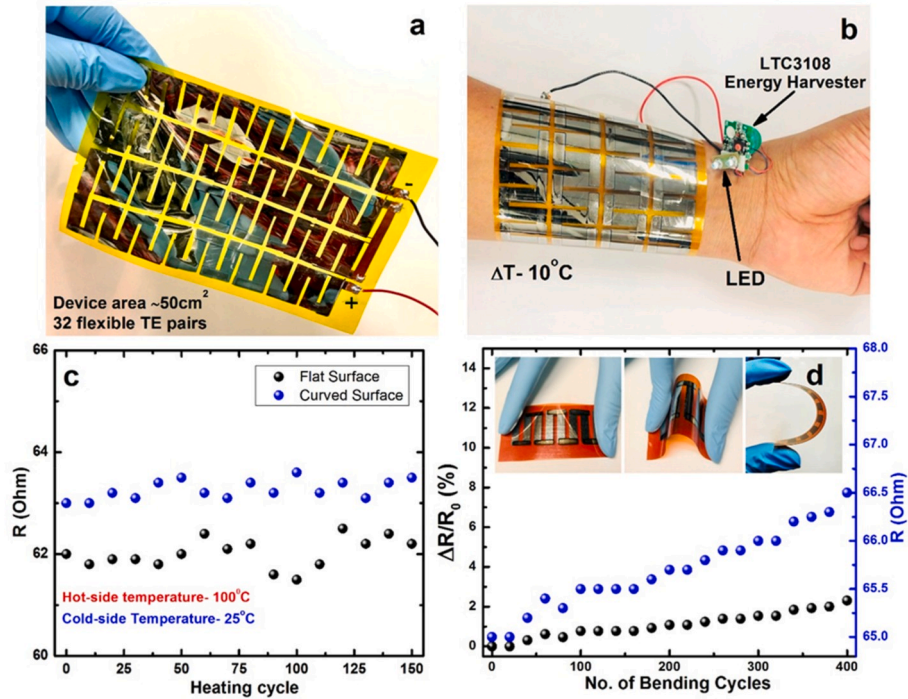


Fig. 5. (a) Fabricated Large-area flexible SnTe-PbTe TEG with 32 TE pairs (b) Real-time demonstration of the TEG as a wearable power source by lighting a LED with body heat (c) Change in internal resistance with the no. of heating cycles (d) Change in TEG internal resistance with no. of bending cycles (bending radius = 3 cm) under ambient temperature.

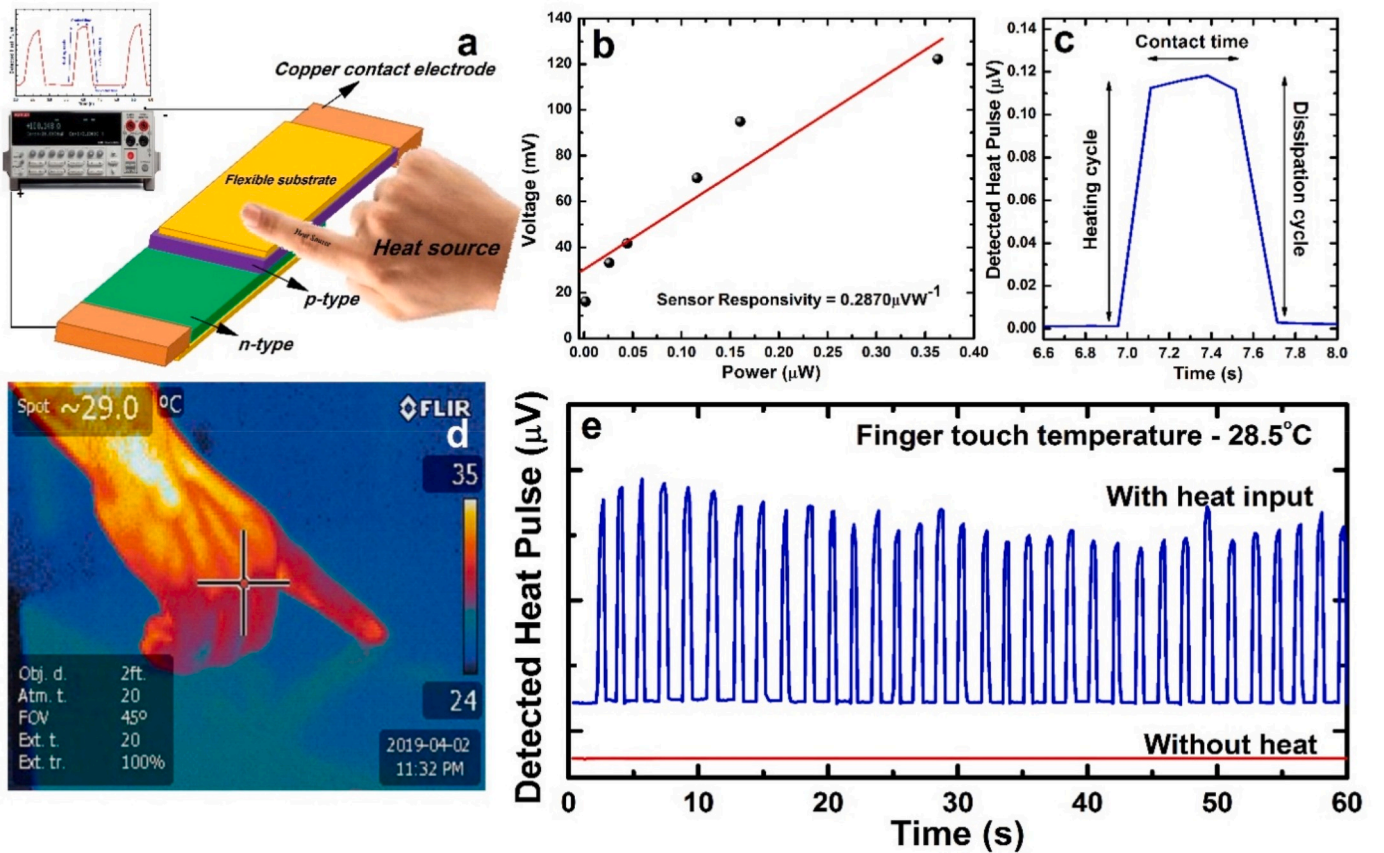


Fig. 6. Thermal touch sensor (a) schematic diagram shows the construction of flexible thermal touch sensor (b) shows the sensor responsivity [25] (c) Electrical response of the heat touch-induced pulse signal [67] (d) IR image of the figure touch (e) compares the electrical pulse signal from the sensor for with and without heat input at ambient atmosphere.

the large Seebeck coefficient and ultra-low thermal conductivity of the thin films. Thus we demonstrate the performance of flexible SnTe/PbTe thin films as an efficient thermal touch sensor.

4. Conclusion

In summary, we have fabricated an in-plane flexible p-SnTe/n-PbTe metal telluride based thermoelectric generator with detailed electrical and thermal investigations on the deposited thin films. Surface roughness profile from the AFM measurement reveals the enhancement in the electrical properties. Temperature-dependent hall measurement exhibits the interrelationship between the surface roughness and the carrier mobility process in thin film. Thermoelectric performance of the deposited thin film exhibits maximum zT of ~ 0.3 (p-type) and ~ 0.2 (n-type) at 550 K. From the fabricated TEGs, maximum output voltage and power density of 250 mV and 8.4 mW/cm^2 at a temperature difference of 120°C . The efficient TEG construction design overcomes the issue of maintaining a large temperature gradient (ΔT). Total average figure of merit (zT_{avg}) and efficiency (η) of the TEG is calculated as 0.2 and $\sim 3\%$. We have also demonstrated multi-scale use of TEG as a wearable electronic power source and industrial waste heat recovery device. The infrared images show the heat transfer between the surface and flexible TEG device interface. Further the performance of the thermal touch sensor demonstrates efficient heat sensitivity of the thin films. The performance of the deposited thermoelectric films and device can be further improved by increasing the active area and electrical properties.

Declaration of competing interest

Authors have no conflict interest for this article.

CRediT authorship contribution statement

Vaithinathan Karthikeyan: Conceptualization, Methodology, Writing - original draft. **James Utama Surjadi:** Conceptualization, Methodology, Writing - original draft. **Joseph C.K. Wong:** Visualization, Investigation. **Venkataraman Kannan:** Visualization, Investigation. **Kwok-Ho Lam:** Writing - review & editing. **Xianfeng Chen:** Writing - review & editing. **Yang Lu:** Resources, Validation, Supervision. **Vellaisamy A.L. Roy:** Resources, Validation, Supervision.

Acknowledgment

We acknowledge grants from the Research Grants Council of Hong Kong Special Administrative Region Project no: T42-103/16N and Environmental & Conservation Fund (ECF) project number 44/2014.

Appendix A. Supplementary data

Supplementary data to this article can be found online at <https://doi.org/10.1016/j.jpowsour.2020.227983>.

References

- [1] T. Ray, J. Choi, J. Reeder, S.P. Lee, A.J. Aranyosi, R. Ghaffari, J.A. Rogers, Soft, skin-interfaced wearable systems for sports science and analytics, *Curr. Opin. Biomed. Eng.* 9 (2019) 47–56, <https://doi.org/10.1016/j.cobme.2019.01.003>.
- [2] Y. Du, J. Xu, B. Paul, P. Eklund, Flexible thermoelectric materials and devices, *Appl. Mater. Today* 12 (2018) 366–388, <https://doi.org/10.1016/j.apmt.2018.07.004>.
- [3] C.-C. Yu, H. Wu, P.-Y. Deng, M.T. Agne, G.J. Snyder, J.P. Chu, Thin-film metallic glass: an effective diffusion barrier for Se-doped AgSbTe₂ thermoelectric modules, *Sci. Rep.* 7 (2017) 45177, <https://doi.org/10.1038/srep45177>.
- [4] W. Wu, H. Haick, Materials and wearable devices for autonomous monitoring of physiological markers, *Adv. Mater.* 30 (2018) 1–17, <https://doi.org/10.1002/adma.201705024>.
- [5] F. Zhang, Y. Zang, D. Huang, C.A. Di, D. Zhu, Flexible and self-powered temperature-pressure dual-parameter sensors using microstructure-frame-supported organic thermoelectric materials, *Nat. Commun.* 6 (2015) 1–10, <https://doi.org/10.1038/ncomms9356>.
- [6] Y. Wang, Y. Shi, D. Mei, Z. Chen, Wearable thermoelectric generator for harvesting heat on the curved human wrist, *Appl. Energy* 205 (2017) 710–719, <https://doi.org/10.1016/j.apenergy.2017.08.117>.
- [7] W.C. Cho, K.Y. Lee, S.B. Yang, What makes you feel attached to smartwatches? The stimulus–organism–response (S–O–R) perspectives, *Inf. Technol. People* 32 (2019) 319–343, <https://doi.org/10.1108/ITP-05-2017-0152>.
- [8] C.S. Kim, G.S. Lee, H. Choi, Y.J. Kim, H.M. Yang, S.H. Lim, S.G. Lee, B.J. Cho, Structural design of a flexible thermoelectric power generator for wearable applications, *Appl. Energy* 214 (2018) 131–138, <https://doi.org/10.1016/j.apenergy.2018.01.074>.
- [9] M. Henriksen, K. Vaagsaether, J. Lundberg, S. Forseth, D. Bjerketved, Explosion characteristics for Li-ion battery electrolytes at elevated temperatures, *J. Hazard Mater.* 371 (2019) 1–7, <https://doi.org/10.1016/j.jhazmat.2019.02.108>.
- [10] H. Yuan, T. Lei, Y. Qin, R. Yang, Flexible electronic skins based on piezoelectric nanogenerators and piezotronics, *Nano Energy* 59 (2019) 84–90, <https://doi.org/10.1016/j.nanoen.2019.01.072>.
- [11] S. He, W. Dong, Y. Guo, L. Guan, H. Xiao, H. Liu, Piezoelectric thin film on glass fiber fabric with structural hierarchy: an approach to high-performance, superflexible, cost-effective, and large-scale nanogenerators, *Nano Energy* 59 (2019) 745–753, <https://doi.org/10.1016/j.nanoen.2019.03.025>.
- [12] H. Guan, T. Zhong, H. He, T. Zhao, L. Xing, Y. Zhang, X. Xue, A self-powered wearable sweat-evaporation-biosensing analyzer for building sports big data, *Nano Energy* 59 (2019) 754–761, <https://doi.org/10.1016/j.nanoen.2019.03.026>.
- [13] X. Zhao, W. Han, C. Zhao, S. Wang, F. Kong, X. Ji, Z. Li, X. Shen, Fabrication of transparent paper-based flexible thermoelectric generator for wearable energy harvester using modified distributor printing technology, *ACS Appl. Mater. Interfaces* 11 (2019) 10301–10309, <https://doi.org/10.1021/acsami.8b21716>.
- [14] R.A. Kishore, A. Nozariasbmarz, B. Poudel, M. Sanghadasa, S. Priya, Ultra-high performance wearable thermoelectric coolers with less materials, *Nat. Commun.* 10 (2019) 1–13, <https://doi.org/10.1038/s41467-019-09707-8>.
- [15] T. Sugahara, Y. Ekubaru, N. Van Nong, N. Kagami, K. Ohata, L.T. Hung, M. Okajima, S. Nambu, K. Suganuma, Fabrication with semiconductor packaging technologies and characterization of a large-scale flexible thermoelectric module, *Adv. Mater. Technol.* 4 (2019) 1–5, <https://doi.org/10.1002/admt.201800556>.
- [16] C. Gayner, K.K. Kar, Recent advances in thermoelectric materials, *Prog. Mater. Sci.* (2016), <https://doi.org/10.1016/j.pmatsci.2016.07.002>.
- [17] Q. Zhang, J. Liao, Y. Tang, M. Gu, C. Ming, P. Qiu, S. Bai, X. Shi, C. Uher, L. Chen, Realizing thermoelectric conversion efficiency of 12% in Bismuth Telluride/Skutterudite segmented modules through full-parameter optimization and energy-loss minimized integration, *Energy Environ. Sci.* 10 (2017) 956–963, <https://doi.org/10.1039/C7EE00447H>.
- [18] D.K. Aswal, R. Basu, A. Singh, Key issues in development of thermoelectric power generators: high figure-of-merit materials and their highly conducting interfaces with metallic interconnects, *Energy Convers. Manag.* (2016), <https://doi.org/10.1016/j.enconman.2016.01.065>.
- [19] Y. Pei, H. Wang, G.J. Snyder, Band engineering of thermoelectric materials, *Adv. Mater.* 24 (2012) 6125–6135, <https://doi.org/10.1002/adma.201202919>.
- [20] M. Hyland, H. Hunter, J. Liu, E. Veety, D. Vashae, Wearable thermoelectric generators for human body heat harvesting, *Appl. Energy* 182 (2016) 518–524, <https://doi.org/10.1016/j.apenergy.2016.08.150>.
- [21] E.I. Rogacheva, O.N. Nashchekina, I.A. Korzh, L.G. Voinova, I.M. Krivulkin, Temperature Dependences of Electrical Resistivity and Thermoelectric, 4355, 2001, pp. 182–187, <https://doi.org/10.1117/12.417781>.
- [22] P.H. Le, C.W. Luo, Thermoelectric and topological insulator bismuth chalcogenide thin films grown using pulsed laser deposition, *Appl. Laser Ablation - Thin Film Depos. Nanomater. Synth. Surf. Modif.* (2016), <https://doi.org/10.5772/65898>.
- [23] G. Tang, K. Cai, J. Cui, J. Yin, S. Shen, Preparation and Thermoelectric Properties of MoS₂/Bi₂Te₃ Nanocomposites, 2016, <https://doi.org/10.1016/j.ceramint.2016.07.083>.
- [24] C.J. An, Y.H. Kang, H. Song, Y. Jeong, S.Y. Cho, Highly integrated and flexible thermoelectric module fabricated by brush-cast doping of a highly aligned carbon nanotube web, *ACS Appl. Energy Mater.* 2 (2018) 1093–1101, <https://doi.org/10.1021/acsaeam.8b01673>.
- [25] E.M.F. Vieira, J. Figueira, A.L. Pires, J. Grilo, M.F. Silva, A.M. Pereira, L. M. Goncalves, Enhanced thermoelectric properties of Sb₂Te₃ and Bi₂Te₃ films for flexible thermal sensors, *J. Alloys Compd.* 774 (2019) 1102–1116, <https://doi.org/10.1016/j.jallcom.2018.09.324>.
- [26] C. Morales, E. Flores, J.R. Ares, C. Sánchez, I.J. Ferrer, Improving the efficiency of thin film thermoelectric generators under constant heat flux by using substrates of low thermal conductivity, *Phys. Status Solidi Rapid Res. Lett.* 12 (2018) 1–6, <https://doi.org/10.1002/pssr.201800277>.
- [27] Y.C. Tseng, H. Lee, N.Y. Hau, S.P. Feng, C.M. Chen, Electrodeposition of Ni on Bi₂Te₃ and interfacial reaction between Sn and Ni-coated Bi₂Te₃, *J. Electron. Mater.* 47 (2018) 27–34, <https://doi.org/10.1007/s11664-017-5777-1>.
- [28] T. Varghese, C. Hollar, J. Richardson, N. Kempf, C. Han, P. Gamarachchi, D. Estrada, R.J. Mehta, Y. Zhang, High-performance and flexible thermoelectric films by screen printing solution-processed nanoplate crystals, *Sci. Rep.* 6 (2016) 6–11, <https://doi.org/10.1038/srep33135>.
- [29] S.H. Park, S. Jo, B. Kwon, F. Kim, H.W. Ban, J.E. Lee, D.H. Gu, S.H. Lee, Y. Hwang, J.S. Kim, D. Bin Hyun, S. Lee, K.J. Choi, W. Jo, J.S. Son, High-performance shape-engineerable thermoelectric painting, *Nat. Commun.* 7 (2016) 1–10, <https://doi.org/10.1038/ncomms13403>.
- [30] C.J. An, Y.H. Kang, H. Song, Y. Jeong, S.Y. Cho, Highly integrated and flexible thermoelectric module fabricated by brush-cast doping of a highly aligned carbon

- nanotube web, ACS Appl. Energy Mater. 2 (2018) 1093–1101, <https://doi.org/10.1021/acsaelm.8b01673>.
- [31] Z. Lu, M. Layani, X. Zhao, L.P. Tan, T. Sun, S. Fan, Q. Yan, S. Magdassi, H.H. Hng, Fabrication of flexible thermoelectric thin film devices by inkjet printing, Small 10 (2014) 3551–3554, <https://doi.org/10.1002/sml.201303126>.
- [32] D. Kong, W. Zhu, Z. Guo, Y. Deng, High-performance flexible Bi₂Te₃ films based wearable thermoelectric generator for energy harvesting, Energy 175 (2019) 292–299, <https://doi.org/10.1016/j.energy.2019.03.060>.
- [33] D. Bourgault, C. Giroud-Garampon, N. Caillault, L. Carbone, Thermoelectrical devices based on bismuth-telluride thin films deposited by direct current magnetron sputtering process, Sensors Actuators A Phys 273 (2018) 84–89, <https://doi.org/10.1016/j.sna.2018.02.015>.
- [34] J.P. Carmo, L.M. Gonçalves, R.F. Wolffenbuttel, J.H. Correia, A planar thermoelectric power generator for integration in wearable microsystems, Sensors Actuators A Phys 161 (2010) 199–204, <https://doi.org/10.1016/j.sna.2010.05.010>.
- [35] N.-W. Park, T.-H. Park, J.-Y. Ahn, S.-H. Kang, W.-Y. Lee, Y.-G. Yoon, S.-G. Yoon, S.-K. Lee, Thermoelectric characterization and fabrication of nanostructured p-type Bi_{0.5}Sb_{1.5}Te₃ and n-type Bi₂Te₃ thin film thermoelectric energy generator with an in-plane planar structure, AIP Adv. 6 (2016) 65123, <https://doi.org/10.1063/1.4955000>.
- [36] D. Zhao, G. Tan, A review of thermoelectric cooling: materials, modeling and applications, Appl. Therm. Eng. (2014), <https://doi.org/10.1016/j.applthermaleng.2014.01.074>.
- [37] S. Twaah, J. Zhu, Y. Yan, B. Li, A Comprehensive Review of Thermoelectric Technology: Materials, Applications, Modelling and Performance Improvement, 2016, <https://doi.org/10.1016/j.rser.2016.07.034>.
- [38] R.B. Schoolar, J.R. Dixon, Optical properties of tin telluride in the visible and infrared regions, J. Opt. Soc. Am. 58 (2008) 119, <https://doi.org/10.1364/josa.58.000119>.
- [39] Y. Pei, X. Shi, A. LaLonde, H. Wang, L. Chen, G.J. Snyder, Convergence of electronic bands for high performance bulk thermoelectrics, Nature 473 (2011) 66–69, <https://doi.org/10.1038/nature09996>.
- [40] G. Tan, L.D. Zhao, F. Shi, J.W. Doak, S.H. Lo, H. Sun, C. Wolverton, V.P. Dravid, C. Uher, M.G. Kanatzidis, High thermoelectric performance of p-type SnTe via a synergistic band engineering and nanostructuring approach, J. Am. Chem. Soc. 136 (2014) 7006–7017, <https://doi.org/10.1021/ja500860m>.
- [41] N. Wang, D. West, J. Liu, J. Li, Q. Yan, B. Gu, S.B. Zhang, W. Duan, Microscopic Origin of the P -type Conductivity of the Topological Crystalline Insulator SnTe and the Effect of Pb Alloying, 2014, pp. 1–6, <https://doi.org/10.1103/PhysRevB.89.045142>, 045142.
- [42] U.S. Shenoy, D.K. Bhat, Electronic structure engineering of tin telluride through co-doping of bismuth and indium for high performance thermoelectrics: a synergistic effect leading to a record high room temperature ZT in tin telluride, J. Mater. Chem. C. 7 (2019) 4817–4821, <https://doi.org/10.1039/C9TC01184F>.
- [43] A.D. LaLonde, Y. Pei, H. Wang, G. Jeffrey Snyder, Lead telluride alloy thermoelectrics, Mater. Today 14 (2011) 526–532, [https://doi.org/10.1016/S1369-7021\(11\)70278-4](https://doi.org/10.1016/S1369-7021(11)70278-4).
- [44] Y.-J. Kim, L.-D. Zhao, M.G. Kanatzidis, D.N. Seidman, Analysis of nanoprecipitates in a Na-doped PbTe–SrTe thermoelectric material with a high figure of merit, ACS Appl. Mater. Interfaces 9 (2017) 21791–21797, <https://doi.org/10.1021/acsami.7b04098>.
- [45] D.K. Bhat, S. Shenoy U, High thermoelectric performance of Co-doped tin telluride due to synergistic effect of magnesium and indium, J. Phys. Chem. C 121 (2017) 7123–7130, <https://doi.org/10.1021/acs.jpcc.7b00870>.
- [46] M. Bala, S. Gupta, T.S. Tripathi, S. Varma, S.K. Tripathi, K. Asokan, D.K. Avasthi, Enhancement of thermoelectric power of PbTe:Ag nanocomposite thin films, RSC Adv. 5 (2015) 25887–25895, <https://doi.org/10.1039/C5RA01000D>.
- [47] S. Xu, W. Zhu, H. Zhao, L. Xu, P. Sheng, G. Zhao, Y. Deng, Enhanced thermoelectric performance of SnTe thin film through designing oriented nanopillar structure, J. Alloys Compd. 737 (2018) 167–173, <https://doi.org/10.1016/j.jallcom.2017.12.011>.
- [48] M.H. Lee, D.-G. Byeon, J.-S. Rhyee, B. Ryu, Defect chemistry and enhancement of thermoelectric performance in Ag-doped Sn_{1+x}Ag_xTe, J. Mater. Chem. A. 5 (2017), <https://doi.org/10.1039/c6ta09941f>.
- [49] Z. Chen, Z. Jian, W. Li, Y. Chang, B. Ge, R. Hanus, J. Yang, Y. Chen, M. Huang, G. J. Snyder, Y. Pei, Lattice dislocations enhancing thermoelectric PbTe in addition to band convergence, Adv. Mater. 29 (2017), 1606768, <https://doi.org/10.1002/adma.201606768>.
- [50] S. Acharya, J. Pandey, A. Soni, Soft phonon modes driven reduced thermal conductivity in self-compensated Sn_{1.03}Te with Mn doping, Appl. Phys. Lett. 109 (2016) 1–6, <https://doi.org/10.1063/1.4963728>.
- [51] S.P. Zimin, E.S. Gorlachey, A.V. Baranov, S.A. Cherevkov, E. Abramof, P.H. O. Rappl, Raman scattering for lead telluride-based thin film structures, Optic Spectrosc. 117 (2014) 748–752, <https://doi.org/10.1134/S0030400X14110241>.
- [52] H.J. Zhao, M. Yao, Q. Chen, D. Wang, L.J. Wan, Theoretical understanding of adlayer structure, thermal stability and electronic property of graphene molecules, Surf. Sci. 604 (2010) 2091–2097, <https://doi.org/10.1016/j.susc.2010.08.024>.
- [53] Z.-Y. Yang, H.-M. Zhang, C.-J. Yan, S.-S. Li, H.-J. Yan, W.-G. Song, L.-J. Wan, Scanning tunneling microscopy of the formation, transformation, and property of oligothiophene self-organizations on graphite and gold surfaces, Proc. Natl. Acad. Sci. Unit. States Am. 104 (2007), <https://doi.org/10.1073/pnas.0611585104>, 3707 LP – 3712.
- [54] K. Krupski, M. Moors, T. Kobiela, A. Krupski, Structure Determination of Au on Pt (111) Surface: LEED, STM and DFT Study, 2015, pp. 2935–2952, <https://doi.org/10.3390/ma8062935>.
- [55] Z. Wang, Z. Ni, R. Zhao, M. Chen, K. Bi, Y. Chen, The effect of surface roughness on lattice thermal conductivity of silicon nanowires, Phys. B Condens. Matter 406 (2011) 2515–2520, <https://doi.org/10.1016/j.physb.2011.03.046>.
- [56] J.U. Surjadi, L. Gao, K. Cao, R. Fan, Y. Lu, Mechanical enhancement of core-shell microlattices through high-entropy alloy coating, Sci. Rep. 8 (2018) 5442, <https://doi.org/10.1038/s41598-018-23857-7>.
- [57] J.Y. Oh, J.H. Lee, S.W. Han, S.S. Chae, E.J. Bae, Y.H. Kang, W.J. Choi, S.Y. Cho, J.-O. Lee, H.K. Baik, T. Il Lee, Chemically exfoliated transition metal dichalcogenide nanosheet-based wearable thermoelectric generators, Energy Environ. Sci. 9 (2016) 1696–1705, <https://doi.org/10.1039/C5EE03813H>.
- [58] G. Micocci, A. Tepore, R. Rella, P. Siciliano, Electrical properties of vacuum-deposited polycrystalline InSe thin films, Sol. Energy Mater. 22 (1991) 215–222, [https://doi.org/10.1016/0165-1633\(91\)90019-H](https://doi.org/10.1016/0165-1633(91)90019-H).
- [59] N. Hansen, Hall-petch relation and boundary strengthening, Scripta Mater. 51 (2004) 801–806, <https://doi.org/10.1016/j.scriptamat.2004.06.002>.
- [60] C. Chiritescu, C. Mortensen, D.G. Cahill, D. Johnson, P. Zschack, Lower limit to the lattice thermal conductivity of nanostructured Bi₂Te₃-based materials, J. Appl. Phys. 106 (2009), <https://doi.org/10.1063/1.3226884>.
- [61] P. Wanarattikan, P. Jitthamapirom, R. Sakdanuphab, A. Sakulkalavek, Effect of grain size and film thickness on the thermoelectric properties of flexible Sb₂Te₃ thin films, Adv. Mater. Sci. Eng. (2019), <https://doi.org/10.1155/2019/6954918>, 2019.
- [62] G.J. Snyder, A.H. Snyder, Figure of merit ZT of a thermoelectric device defined from materials properties, Energy Environ. Sci. 10 (2017) 2280–2283, <https://doi.org/10.1039/c7ee02007d>.
- [63] H.S. Kim, W. Liu, Z. Ren, The bridge between the materials and devices of thermoelectric power generators, Energy Environ. Sci. 10 (2017) 69–85, <https://doi.org/10.1039/c6ee02488b>.
- [64] A. Hmood, A. Kadhimi, H. Abu Hassan, Lead–ytterbium–telluride thin films prepared using thermal evaporation technique for thermal sensing applications, Superlattice. Microst. 54 (2013) 204–214, <https://doi.org/10.1016/j.spmi.2012.11.015>.
- [65] C. Wan, R. Tian, A.B. Azizi, Y. Huang, Q. Wei, R. Sasai, S. Wasusate, T. Ishida, K. Koumoto, Flexible thermoelectric foil for wearable energy harvesting, Nano Energy 30 (2016) 840–845, <https://doi.org/10.1016/j.nanoen.2016.09.011>.
- [66] C. Xie, Interactive heat transfer simulations for everyone, Phys. Teach. 50 (2012) 237–240, <https://doi.org/10.1119/1.3694080>.
- [67] M. Ruoho, T. Juntunen, T. Alasaarela, M. Pudas, I. Tittonen, Transparent, flexible, and passive thermal touch panel, Adv. Mater. Technol. 1 (2016), <https://doi.org/10.1002/admt.201600204>.